International Journal of Heat and Mass Transfer 112 (2017) 343–353

Contents lists available at ScienceDirect

International Journal of Heat and Mass Transfer

journal homepage: www.elsevier.com/locate/ijhmt

Multi-artery heat-pipe spreader: monolayer-wick receding meniscus transitions and optimal performance

Minki Kim, Massoud Kaviany *

Department of Mechanical Engineering, University of Michigan, Ann Arbor, MI 48109, USA

ARTICLE INFO

Article history:
Received 18 February 2017
Received in revised form 16 April 2017
Accepted 20 April 2017

Keywords:
Multi-artery heat pipe spreader
Heterogeneous monolayer wicks
Network model
Meniscus transition
Local dryout
Figure of merit
Superheat range

ABSTRACT

For high heat flux and low thermal resistance, the multiple-artery heat-pipe spreader uses distributed high-permeability arteries (posts) for liquid supply and high-capillary pressure monolayer wick for liquid spreading and evaporation. Experiments indicate the receding meniscus transitions in monolayer play a role in sudden drop in thermal resistance prior to dryout. Using monolayer SEM images and the minimum surface energy principles, the meniscus dynamics up to dryout is analyzed, and the meniscus location, capillary pressure, effective thermal conductivity, and permeability are also predicted for heterogeneous, periodic sintered copper-particle (including bimodal particle size) unit cells. The liquid thickness is nonuniform within the heterogeneous unit cell, and with increase in the wick superheat local dryout occurs (meniscus snaps) in the loose-packed region influencing the wet-wick properties and the occurrence of the minimum thermal resistance. The monolayer wick continues to function under local dryout (away from post) until a receding dry front is formed followed by complete dryout. These predictions are in good agreement with experiments. The optimal wick thermal-hydraulic performance, i.e., dimensionless ratio of heat flux to thermal resistance (wick figure of merit Z_m) is sought through analysis. The uniform, sintered, close-packed 30–50 μm particles give the highest Z_m over a range of superheat in the wet regime, and 30 μm particles give a record low resistance near 2.5 μK/(W/m^2)

1. Introduction

Improvements in passive and active liquid supply in thermal management aims at increase in heat flux load and decrease thermal resistance. Specifically, capillary-driven liquid flow has been widely used to supply liquid (similar to heat pipe) without use of electric power. To enhance the heat transfer limit (critical heat flux), it is essential to decrease the liquid pressure loss, and various porous structures such as micropost arrays [1–3], columns (posts) [4], converging lateral arteries [5], and biporous wicks [6,7] have been used.

Multiple-artery heat-pipe spreader (MAHPS) is a heat pipe with large and spread vapor space and generally a smaller heated (evaporation) area compared to the condenser section with distributed liquid arteries [8]. In the MAHPS, Fig. 1, capillary-driven liquid flow begins in the condenser, through screen layer, then posts (liquid artery), and finally to the monolayer wicks. In screen-post-monolayer unit cell, the capillary pressure has a maximum value at the monolayer cell boundary, where the liquid thickness $\delta_{l,m}$ is minimum. While spreading over the monolayer wick, the liquid evaporates at the liquid surface (meniscus). For heat removal, the cooling water flows in the opposite side of condenser.

The thermal-hydraulics of MAHPS has been predicted by Min et al. [8] and Hwang et al. [4,5], using network model with its geometrical parameters. Min et al. [8] showed that overall thermal resistance in MAHPS increases with an increase in artery (post) diameter. They also compared performance with uniform wick and predicted the improved performance by MAHPS. In experiments by [4,5] using the screen-post and lateral artery for liquid supply, respectively, and monolayer wicks for capillarity, the slope of thermal resistance-superheat is positive as generally expected. However, for $q > 250$ W/cm^2, the resistance increases rapidly up to 320 W/cm^2 with decrease in superheat and for $q > 320$ W/cm^2, the thermal resistance recovers the general trend. This nonlinear resistance has been reported by [2,9–12] using copper powder wicks and by [6,9,11,13–16] using biporous wicks and media, but not observed in other wicks [3,17] with finger-like liquid supply [5]. This transition has been related to the onset of nucleate boiling [9,10,14,15], or meniscus transitions in heterogeneous monolayer wick [4,12], however, quantitative explanation has not been provided yet.

In this study, we explain this transition (nonlinear pattern) through the heterogeneous structure of the monolayer, as revealed

---

* Corresponding author.
E-mail address: kaviany@umich.edu (M. Kaviany).

http://dx.doi.org/10.1016/j.ijheatmasstransfer.2017.04.131
0017-9310/

Nomenclature

A	area (m^2)
a	surface area to unit volume ratio (m^{-1})
C_J	constant for Leverett *J*-function
c_p	heat capacity (J/kg-K)
D, d	diameter (m)
f	friction factor
g	gravitational acceleration (m/s^2)
H	height (m)
Δh_{lg}	heat of evaporation (kJ/kg)
J	Leverett *J*-function
K	permeability (m^2)
k	thermal conductivity (W/m-K)
L	length, pitch, thickness (m)
M	mass (kg)
m	molecular weight (g/mol)
N_p	packing number
n_{sh}	number density of shute wire (wires/m)
n_{wa}	number density of warp wire (wires/m)
p	pressure (Pa)
Q	heat flow rate (W)
q	heat flux (W/m^2)
R	thermal resistance (K/W)
R_g	universal gas constant (J/mol-K)
Re	Reynolds number
r	radial location (m)
S	mean crimping factor
s	substrate, saturation in lg
T	temperature (K)
w	width (m)
Z_m	dimensionless figure of merit
z	Melros function
$\langle\rangle$	average

Greek symbols

α	tortuosity factor
Δ	difference, drop
δ_l	liquid thickness (m)
ϵ	porosity
μ	viscosity (Pa-s)
ρ	density (kg/m^3)
σ	surface tension (N/m)
θ_c	contact angle (°)

Subscripts

ave	average packing
b	bulk
CHF	critical heat flux
Cu	copper
c	capillary, condenser, cooling, cross
cl	close-packed
c-v	capillary-viscous
e	effective, evaporator
g	gas
h	heated
i	index of node
k	kinetic limit
l	liquid
lg	liquid-gas phase change
lo	loose-packed
m	monolayer wicks
multi	multi-node
N	total number of nodes
o	baseline
p	post (artery)
po	pore
s	screen mesh, surface
sh	shute wire
t	thermal
u	fluid flow
up	upper layer
wa	warp wire
Z	Zuber
$\updownarrow$	across
$\leftrightarrow$	along

from SEM images, and define various regimes associated with it. We use minimum surface energy principle to track the receding monolayer meniscus and find the effective properties by solving numerically the liquid flow and heat transfer in monolayer unit cell. We then solve governing equations of the screen-post-monolayer unit cell using single- and multi-node network models. With the heterogeneous unit cell, the network models predict degrade of performance compared to the homogeneous unit cell. To improve the heat transfer limit caused by the spatial heterogeneity, we also seek and find the homogenous monolayer wick structure for optimal heat transfer performance: highest figure of merit and lowest thermal resistance.

2. Methods

2.1. Direct simulations of monolayer unit cell

The monolayer wick unit cell is defined, based on the SEM micrographs (Tescan MIRA3 FEG SEM) (Fig. 2(a,b)). There are sporadic multi-layer coatings and particle diameter variations as well as close- to loose-packed regions (Fig. 2(c)). The average porosity is estimated using image-processing software (Image J) and is $\langle\epsilon_m\rangle = 0.58$ with average diameter $\langle d_m\rangle = 50\ \mu m$ (Fig. 2(b)). As shown in Fig. 2(a,b), the multi-layered structure with particle size variation and sintering consolidation represents monolayer heterogeneous unit cell (varying local packing and porosity) [18]. The local porosity ranges from less than 0.5 to over 0.8 (Figs. 2(a, b)), and are considered to determine the heterogeneous unit cell in close- to loose-packed regions (Fig. 2(c)). The selection represents the observations on several SEM monographs and consequently explains the nonlinear thermal resistance in the experiment. The copper particles are slightly sintered and consolidated with each other since they have original spherical shape without shape distortion (Fig. 2(b, top)). However, particles are sintered more with the substrate and have truncated portion in the lower hemisphere (Fig. 2(b, bottom)). For improved water wettability, thermal oxidation is used and results in contact angle $\theta_c = 43 \pm 6^\circ$ [4,5]. The heterogeneous unit cell is shown in Fig. 2(c) and consists of square array of particles with a diameter $d_{m,o}$ in baseline with a portion having smaller particle with a diameter $d_{m,up}$ on top. The permeability is anisotropic and has the x and y-directional flows (Fig. 2(c)). Sintering consolidation is modeled with connecting cylinders of a diameter of $0.2d_{m,o}$, and the lower hemisphere of particles are truncated as sintered to the substrate with a depth of $0.1d_{m,o}$. The reduced, square periodic unit cell in average packing region has $l_x = l_y, = 1.49d_{m,o}$ with $\epsilon_{ave} = 0.58$

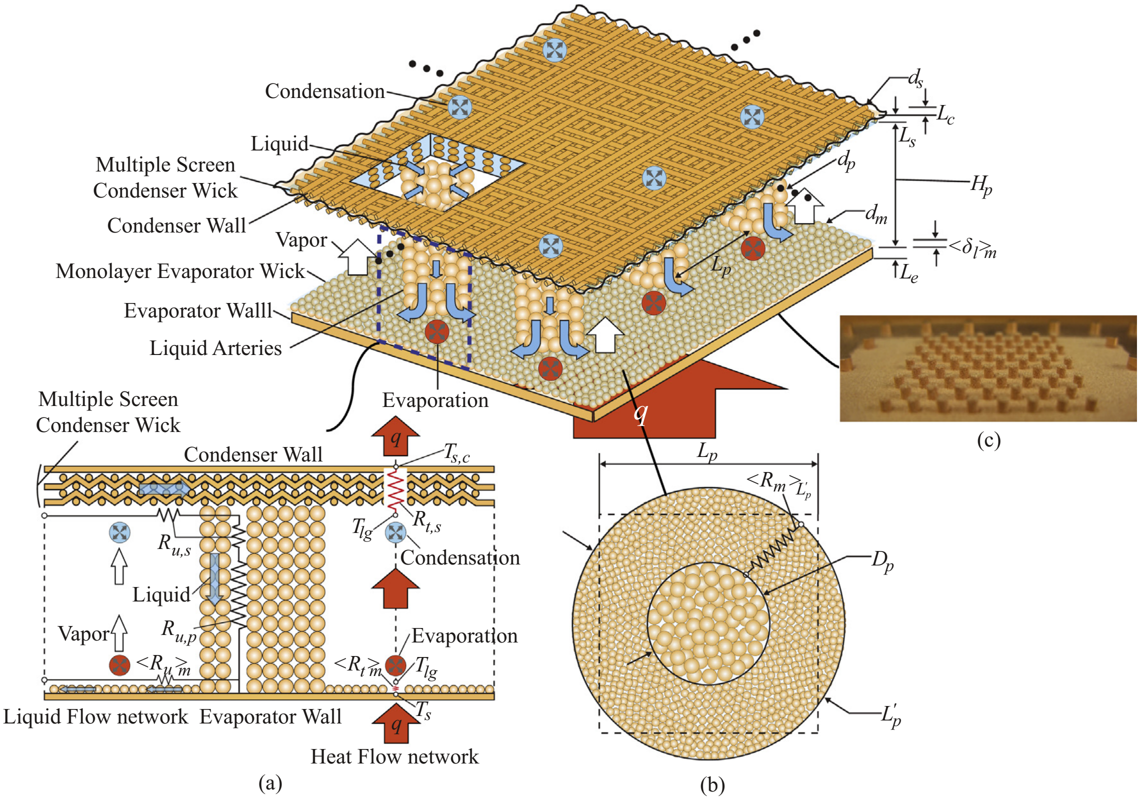

Fig. 1. A schematic of multiple-artery heat pipe spreader (MAHPS) with geometric parameters. While heat is transferred from the substrate to the liquid free surface in monolayer and leads to liquid evaporation, that vapor is condensed in the screen layer and returned through the posts. (a) A network model for heat and liquid flow, (b) a screen-post-monolayer unit cell, and (c) optical images of multiple posts and monolayer used in Hwang et al. [4] are shown. The solid posts on the boundaries in (c) are for mechanical structure purpose.

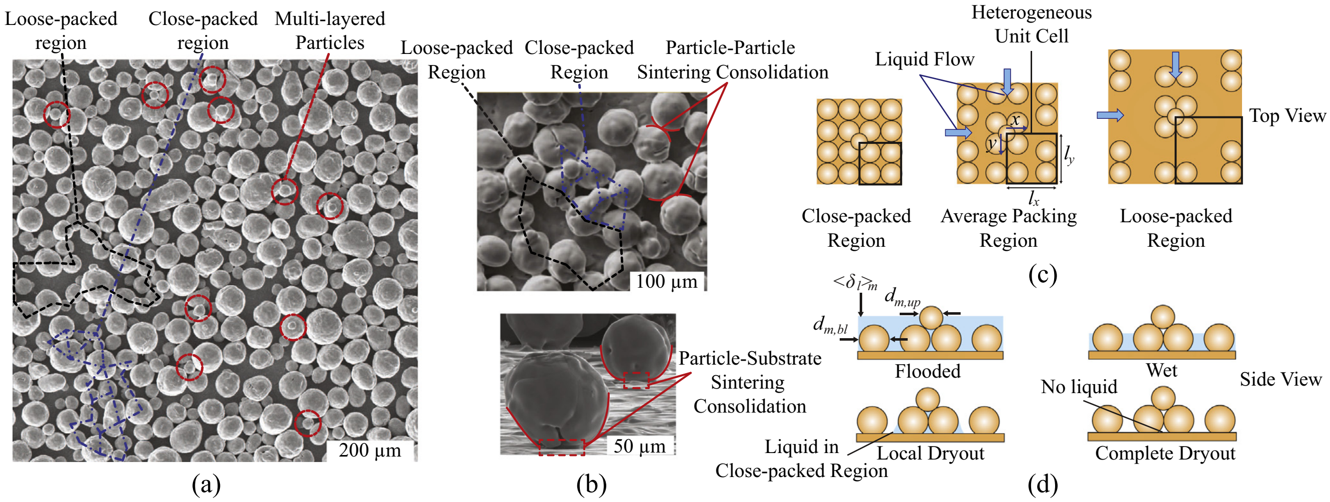

Fig. 2. (a) SEM micrograph of heterogeneous particle distribution in monolayer wicks (top view) [4]. (b) Loose and close-packed regions with sintering consolidation among particles (top view, upper), and between particles and substrate (side view, lower) in SEM micrograph. (c) Top view of monolayer unit cell in close-packed (isotropic), average pakcing, loose-packed (anisotropic) regions. (d) Meniscus recedes from flooded to wet, to local dryout, and to complete dryout regions (side view).

(Fig. 2(c)), which is matched with $\langle\epsilon_m\rangle$ of SEM image. In addition, the close-packed region has $\epsilon_{cl} = 0.47$ ($l_x = l_y, = d_{m,o}$), and the loose-packed region has $\epsilon_{lo} = 0.85$ ($l_x = l_y, = 4.5d_{m,o}$) (Fig. 2(c)).

Liquid content of monolayer wick undergoes variations with the heat flux (Fig. 2(d)). Initially, monolayer is charged with 120% of its thickness [4], and this is called the flooded. With increase in heat flux, the meniscus recedes, capillary flow commences, and the wick remains wet. At yet larger heat flux, the meniscus continues to recede and the loose-packed portion of the wick dries out, and this is called local dryout. This is followed by a complete dryout.

The equilibrium meniscus topology is obtained using the Surface Evolver (SE) based on surface energy minimization [19–23], as applied to periodic, close- and loose-packed particle wick structures [24–27]. Sample close- and loose-packed unit cells are shown

Table 1
MAHPS geometric parameters and conditions in Hwang et al. [4].

Parameter	Magnitude	Parameter	Magnitude
A_c	12×7 mm^2	θ_c	45°
A_h	1×1 mm^2	D_p	2.2 mm
L_p	3.5 mm	d_m	50/40 μm
L'_p	4.0 mm	d_p	150 μm
H_p	2.6 mm	$d_{s,sh}$	66 μm
L_e	2.6 mm	$d_{s,wa}$	66 μm
L_c	1 mm	K_p	12.7 μm^2
L_s	1 mm	ϵ_p	0.35
$D_{s,po}$	0.10 mm	$n_{sh} \times n_{wa}$	145×145 per in^2

in Fig. 2(c) and used in the SE. The geometrical conditions for the spherical particles, substrate, and liquid (including liquid volume fraction) are prescribed. The conjugate gradient method is used to accelerate the gradient descent and refinement of the surface, and iteration steps are repeated for convergence with zero scale factor. The contact angle $\theta_c = 45^\circ$ is for comparison with existing experiment on water and oxidized copper particles [4], and the baseline particle diameter $d_{m,o} = 50$ μm (Table 1). The Bond number, ratio of gravity to surface tension, is about 10^{-4}, so gravity effect is neglected [28]. The SE results are exported to the ANSYS Design Modeler, and the mesh is generated by ANSYS Meshing with the Patch Conforming algorithm using tetrahedral elements. The pressure-based solver under steady-state condition is used for numerical solutions, and the governing equations (continuity, Navier-Stokes, and energy equation) are given as

$$\nabla \cdot \mathbf{u}_l = 0 \tag{1}$$

$$\rho_l \mathbf{u}_l \cdot \nabla \mathbf{u}_l = -\nabla p_l + \mu_l \nabla^2 \mathbf{u}_l \tag{2}$$

$$\rho_l c_{p,l} \mathbf{u}_l \cdot \nabla T_l = k_l \nabla^2 T_l. \tag{3}$$

For liquid flow model, the flow is laminar (and incompressible), and the Reynolds number Re_D is generally smaller than 0.1 [28]. Liquid meniscus is exposed to saturated vapor at shear-free interface, and no-slip condition is applied on solid surfaces with periodic inlet/outlet pressure drop. For a given pressure gradient along the unit cell, the volume-averaged liquid velocity is determined and is used to calculate the monolayer permeability tensor $\mathbf{K}_m$. The Darcy model is employed, which is expressed as

$$-\frac{dp}{dr} = \frac{\mu_l}{K_m} u_l. \tag{4}$$

For heat flow model, adiabatic condition is applied to the vapor-exposed surface of the particles, meniscus is at $T_{lg} = 373$ K, and variable substrate surface superheat $T_s - T_{lg}$. Liquid temperature is the mean temperature of T_{lg} and T_s, and meniscus topology is considered to be static (obtained from the Surface Evolver calculation) because it is found that the convection effect is negligible [12,26,27]. Heat flow rate from the substrate is used to calculate effective thermal conductivity perpendicular to the substrate $\langle k \rangle_m$ employing the Fourier law as

$$Q = \langle q \rangle A_h = \langle k \rangle_m A_h \frac{T_s - T_{lg}}{\langle \delta_l \rangle_m}, \tag{5}$$

where the liquid thickness $\langle \delta_l \rangle_m$ is the surface-averaged $\delta_{l,m}$ over heated area. Representative results for average packing with a liquid thickness of $0.66 d_{m,o}$ are shown in Fig. 3. The liquid flow is different in the x and y direction, and heat transfer is dominated by the high thermal conductivity of copper particles.

Mesh independence of the results was verified using two different mesh size 0.012 and $0.014 d_{m,o}$, with change in $\mathbf{K}_m$ and $\langle k \rangle_m$ smaller than 0.1% for every packing regions. Sintering-area independence study was also performed to verify that the change of diameter of connecting cylinders 0.1, 0.2 and $0.26 d_{m,o}$ between particles results in less than 1% change in $\mathbf{K}_m$ and $\langle k \rangle_m$. Moreover, for sintered area between particle truncated area and the bottom, independence study was performed to verify that small changes of that area do not change $\mathbf{K}_m$ and $\langle k \rangle_m$ significantly. Three different contact areas with diameters of 0.17, 0.2, and $0.23 d_{m,o}$) were considered, and $\mathbf{K}_m$ and $\langle k \rangle_m$ changes are smaller than 3%.

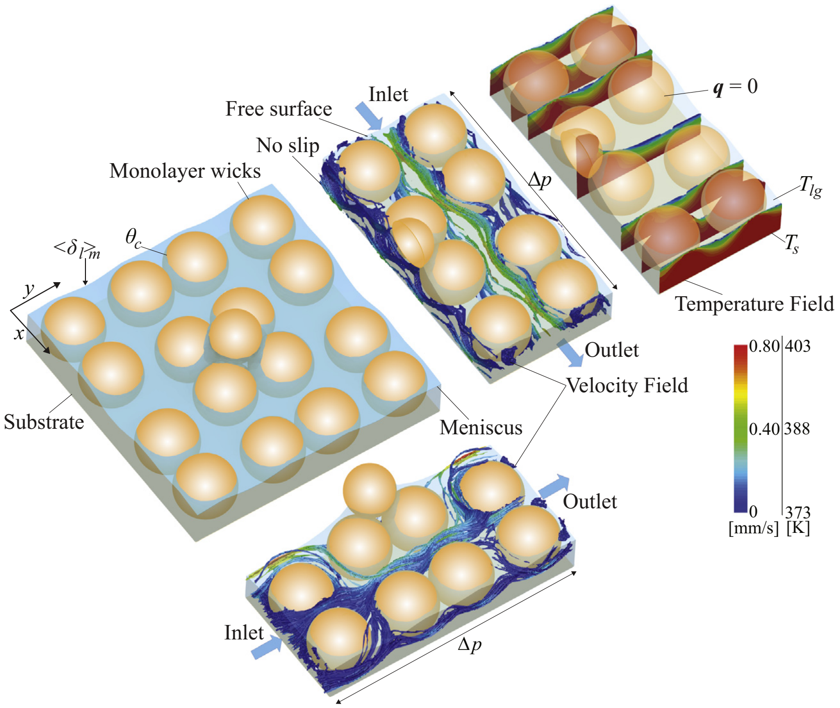

Fig. 3. Typical results of the SE calculations on the heterogeneous unit cell, showing the equilibrium meniscus topology. Typical velocity and temperature fields from the ANSYS FLUENT calculations, using the meniscus from the SE. Due to anisotropy, the pathlines in two principal directions are shown.

2.2. Local volume-averaged analyses of screen-post-monolayer unit cell

The thermal-hydraulic network models [8] are applied to the screen, post, and monolayer wicks (Fig. 1(a)). With the pointwise calculation of local thermal-hydraulic properties as a function of liquid thickness, our multi-node network model improves upon the analysis used in [8]. Local thermal equilibrium between solid and liquid, and between liquid and vapor are assumed under uniform liquid surface temperature, saturation temperature at 1 atm. In addition, using the mean curvature of meniscus, capillary pressure is determined by Young-Laplace equation [29], which is written as

$$p_c = p_g - p_l = \frac{2\sigma}{r_c}\cos\theta_c. \tag{6}$$

The mass conservation for liquid flow is given using the continuity equation as

$$\frac{d(\rho_l u_l)}{dr} + \frac{d(\rho_g u_g)}{dz} = 0. \tag{7}$$

A circular screen-post-wick unit cell is assumed (Fig. 1(b)), with a diameter of L_p' calculated from a square unit cell and is covering the heated area. The monolayer is discretized in radial direction, and for each element, the Darcy law (Eq. (4)) and the Fourier law (Eq. (5)) are employed to calculate pressure drop along the monolayer and the post, and temperature difference across the monolayer. Pressure drop along and across the screen layer are calculated using empirical correlations [30,31] between friction factor (f) and liquid Reynolds number (Re) in horizontal and vertical direction, which can be given as

$$f_{s,\updownarrow} = \frac{8.61}{Re_{s\updownarrow}} + 0.52, \quad f_{s,\leftrightarrow} = \frac{408e^{-2.94N_p}}{Re_{s,\leftrightarrow}}, \tag{8}$$

where N_p is a packing number.

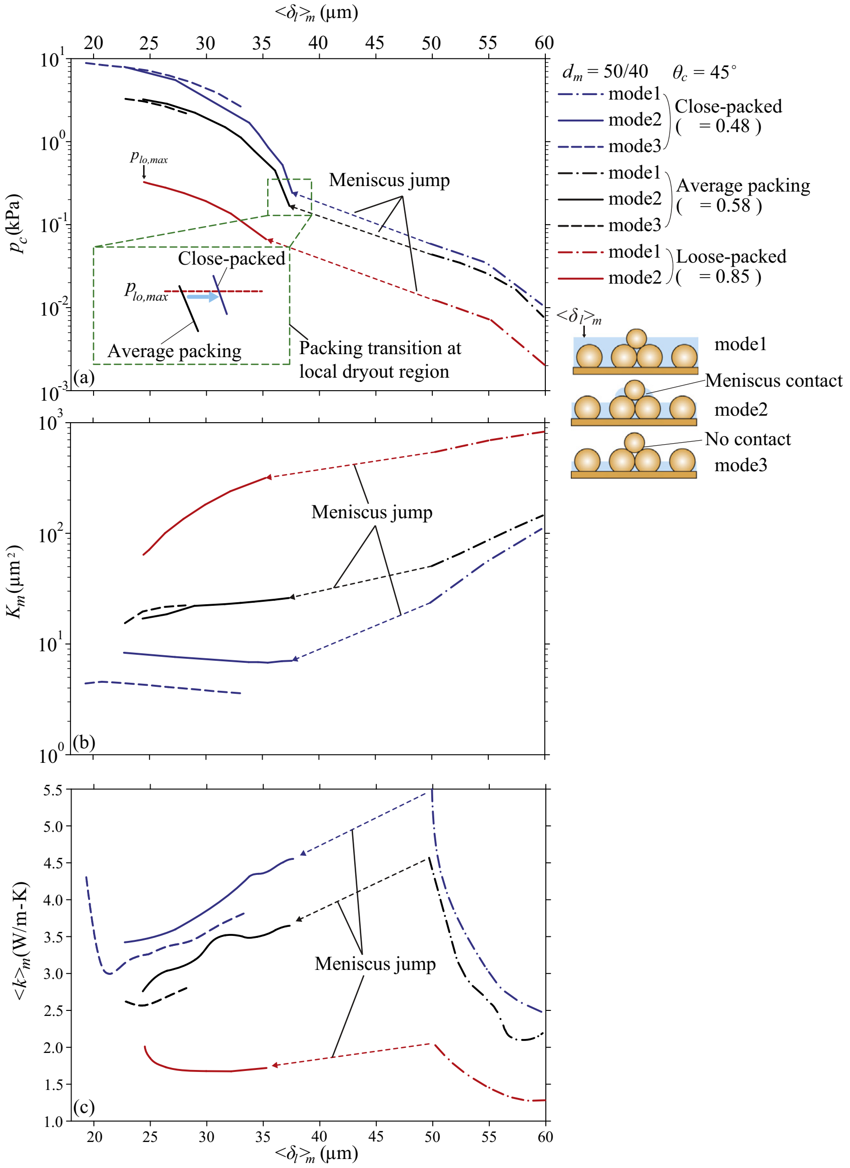

Fig. 4. Variations of predicted (a) capillary pressure, (b) permeability, and (c) thermal conductivity of the heterogenerous unit cell in the monolayer, as a function of average liquid thickness. In the unit cell, particle diameters in baseline and upper layer are 50 and 40 μm, respectively, with a contact angle of 45°. The porosity of close-, average, and loose-packed regions are 0.48, 0.58, and 0.85, respectively.

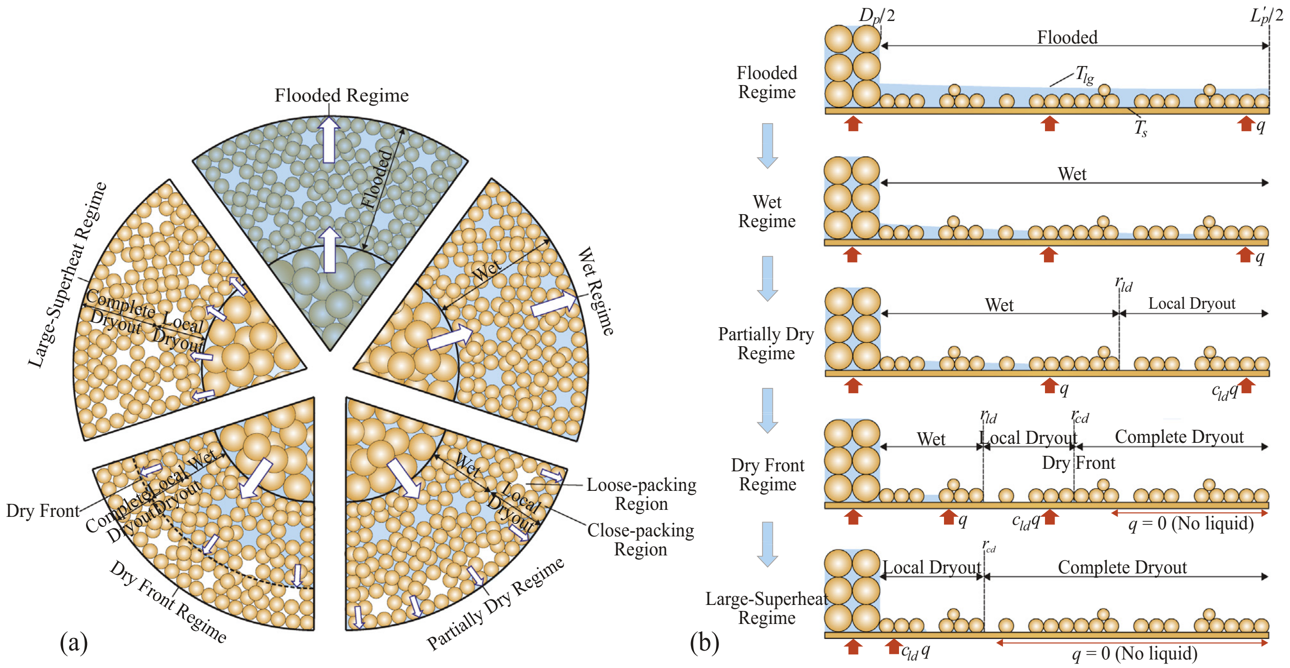

Fig. 5. (a) Top view and (b) side view of five regimes of meniscus receding transitions: Flooded; wet; partially dry; dry front; large-superheat regimes. Receding meniscus dynamics in the heterogeneous unit cell during wet regime can be found in the video (click here, Youtube).

The pore sizes and permeability are chosen such that monolayer capillary pressure can drive the liquid flow with the sum of pressure drop in the screen layer and the post $\Delta p_s + \Delta p_p$ constituting a small portion of the monolayer capillary pressure p_c at its farthest radial location. Weibel et al. [10] visualized bubble generations during boiling in large-sized powder wicks (250–355 μm diameter) with 600 μm wick thickness (different from the screen-post-monolayer wick), however nucleate boiling has not observed in conventional copper-powder wicks and only liquid surface evaporation is addressed in [11] (See Appendix A for details of the multi-node liquid and heat flow network model).

In addition, simple-node model of the screen-post-monolayer using Eqs. (4), (20)–(27) gives

$$q = (p_{m,c} - \Delta p_{s,\updownarrow} - \Delta p_{s,\leftrightarrow})\frac{\rho_l}{\mu_l}\left[\frac{H_p}{K_p A_p} + \left(\frac{(L'_p - D_p)/2}{K_m A_{m,ac}}\right)\right]^{-1}\frac{\Delta h_{lg}}{A_e}, \qquad (9)$$

where $A_e = \pi(L'^2_p - D^2_p)/4$. With no evaporation under posts, the effective heated area A_e is used, and the monolayer liquid flow path is $(L_p - D_p)/2$. Screen wicks pressure drop is divided into cross- and in-plane in Eq. (9).

3. Receding-meniscus transitions in heterogeneous monolayer

Based on the results from SE and numerical simulation, liquid and heat flow network model predicts the experimental study conducted by Hwang et al. [4] using heterogeneous unit cell consisting of bimodal, bi-layered, and sintered particles. In Section 3.1, thermal-hydraulic properties of the heterogeneous unit cell in differently packed region will be described. In Section 3.2, regime transition local dryout caused by receding meniscus will be analyzed by the network model using volume-averaged properties.

3.1. Two-diameter, two-layered, heterogeneous monolayer unit cell

Using SEM images, a heterogeneous unit cell with bi-modal (two particle diameters), two-layered particles is selected with three different packing regions (Fig. 2). In previous studies [12,24–26], a homogeneous, single-layered unit cell has been used. In this unit cell, as the meniscus recedes, the capillary pressure p_c increases and reaches a maximum $p_{c,max}$, followed by decrease till the meniscus contacts with substrate (snaps). For the heterogeneous unit cell, as meniscus recedes, it contacts with the particle on the upper layer and is puckered by diminishing space, while capillary pressure is relatively small (mode 1) (Fig. 4(a)). However, when it reaches to centerline, it also contacts with lower particles, and p_c becomes negative (θ_c of 45°). Since liquid in monolayer is only driven by positive p_c, the meniscus jumps from mode 1 to mode 2. In mode 2 (Fig. 4(a)), the liquid surface is in touch with the particles in both baseline and the upper layer, and the p_c continues to increase until the meniscus at mode 2 reaches the substrate. Specifically, in the close- and average packing region, the meniscus can be also at hydraulic equilibrium when it does not contact with the particle in the upper layer (mode 3). At mode 3, meniscus does not contact with the particles in the upper layer, but is at the hydraulic equilibrium. Mode 2 and 3 of receding meniscus are also found in Hwang et al. [5] and cause a hysteresis in the thermal resistance. As shown in Fig. 4(b), the permeability K_m in all packing regions decreases as meniscus recedes. From the Carman-Kozeny relation (Eq. (27)) of monolayer, the bulk regional permeabilities are $K_{m,cl} = 5$, $K_{m,ave} = 14$, and $K_{m,lo} = 349$ μm², in good agreement with K_m of mode 2 and 3. p_c is inversely proportional to $(K_m/\epsilon_m)^{1/2}$ [32,29] as

$$p_c = J(s)\frac{\sigma\cos\theta_c z(\theta_c)}{(K_m/\epsilon_m)^{1/2}} = C_J\frac{\sigma}{(K_m/\epsilon_m)^{1/2}} \quad \text{for } s = 0, \qquad (10)$$

where J is Leverett J-function of saturation s, and z is melrose function of θ_c. We note that this is generally followed by the calculation (Fig. 4(a,b)). The effective thermal conductivity $\langle k\rangle_m$ varies in the different modes and with $\langle\delta_l\rangle_m$. As meniscus recedes, $\langle k\rangle_m$ increases in mode 3 because liquid volume (low k of water) over the spheres decreases. However, in mode 2, with decrease in $\langle\delta_l\rangle_m$, $\langle k\rangle_m$ in close and average packing regions decrease because of the volume of copper particles (large k of copper) submerged in the liquid decreases. For loose-packed region, $\langle k\rangle_m$ increases as meniscus recedes because of high porosity and large volume of liquid in the unit cell. At mode 1, $\langle k\rangle_m$ shows similar pattern to mode 2, but in the close-packed region, $\langle k\rangle_m$ increases again when meniscus becomes close to the substrate. Comparing with bulk thermal conductivity of monolayer wicks ($\langle k\rangle_{m,b,cl} = 14$, $\langle k\rangle_{m,b,ave} = 6$, and $\langle k\rangle_{m,b,lo}$ = 1 W/m-K), which are obtained by an empirical relation [32] as

$$\langle k\rangle_{m,b} = k_l\left(\frac{k_{Cu}}{k_l}\right)^{0.280-0.757\log\langle\epsilon\rangle_m - 0.057\log\left(\frac{k_{Cu}}{k_l}\right)}, \tag{11}$$

and $\langle k\rangle_m$ from our calculation is within these range of $\langle k\rangle_{m,b}$ (Fig. 4(c)).

3.2. Regime transitions and nonlinear thermal resistance: comparison with reported experiment

As heat flux q is supplied increasingly from the substrate, receding meniscus shows a different behavior with nonlinear thermal resistance in MAHPS [4]. This can be explained by five regimes (flooded, wet, partially dry, dry front, and large-superheat regimes) (Fig. 5) and the transitions between them.

As evaporation is initiated, the heat flux $\langle q\rangle$ increases and thermal resistance $A\langle R_t\rangle_m$ decreases with increase in superheat $\langle T_s - T_{\rm lg}\rangle$ during the first two regimes: flooded and wet regimes (Fig. 6). The liquid charge is initially 120%, so $\langle\delta_l\rangle_m$ starts from $1.2d_{m,o}$ with a small pressure gradient along the wicks. Liquid flows from the post to the boundary of the screen-post-monolayer wicks unit cell (Fig. 5). Once the meniscus loses contact with the top particle ($\langle\delta_l\rangle_m = d_{m,o}$) with a heat flux of 1.7 MW/m^{2}and has transition from mode 1–2 (Fig. 4(a)), p_c becomes significant with onset of the wet regime. In the wet regime, since at mode 2, meniscus $\langle q\rangle$ versus $\langle T_s - T_{\rm lg}\rangle$ is not linear, but $\langle q\rangle$ follows $\langle T_s - T_{\rm lg}\rangle^2$ (Fig. 5(a)) since $\langle\delta_l\rangle_m$ decreases and Δp_m increases promptly with increase in $\langle q\rangle$ during the transition between the flooded and wet regimes (Eq. (22)). This can be derived from Eq. (8) of [4] using scaling analysis and the simple-node network model (Eq. (9)). From the network models (Eqs. (20)–(27)), the heat flow rate Q_i and superheat ΔT_i in the wet regions are calculated using the properties (p_c, K_m, $\langle k\rangle_m$) of monolayer unit cell at the average packing. In this regime, uniform q is assumed and supplied to the whole substrate area including the posts due to the high thermal conductivity of copper substrate. In addition, the dryout effects are not considered in the calculation of $\langle q\rangle$ and $A\langle R_t\rangle_m$, since there are no dryout in these two regimes. The multi-node model is checked with the approximate single-node model (Fig. 6), which neglects the thermal-hydraulic variations in the monolayer.

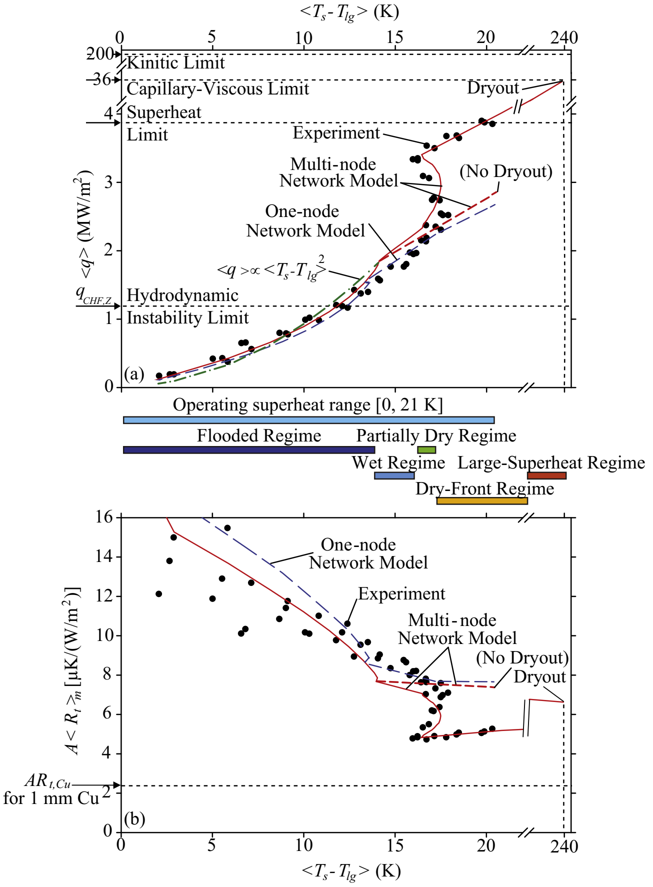

Fig. 6. Dependence of (a) heat flux $\langle q\rangle$ and (b) thermal resistance $A\langle R_t\rangle_m$ on superheat $\langle T_s - T_{\rm lg}\rangle$ for MAHPS. Experimental data and prediction from single- and multi-node network model are shown and compared with hydrodynamic instability, superheat, capillary-viscous, and kinetic limits. With the MAHPS operating superheat range (0–20 K), flooded, wet, partially dry, dry front, and large-superheat regimes are shown.

For $\langle q\rangle > 2.3$ MW/m^2 and $\langle\delta_l\rangle_m = 0.74d_{m,o}$, as the meniscus locally contacts the substrate at the loose-packed region, local dryout in the monolayer wick occurs (Fig. 2(d)), and partially dry regime becomes started, as observed by Wong et al. [11]. During first two regimes, p_c follows the thermal-hydraulic properties of average-packed region. However, with the regime transition from wet to partially dry regime, p_c reaches maximum capillary pressure of the unit cell at loose-packed region, $p_{lo,max}$ (green dotted box in Fig. 4(a)). In the local dryout region, the liquid is confined to the close-packed region with unstable meniscus intermittently moving back and forth towards the loose-packed region [33]. The meniscus at local dryout region follows the properties of close-packed region (shown in Fig. 4(a)), not average packing region (packing transition). In the monolayer, it is assumed that the meniscus has a maximum capillary pressure $p_{lo,max}$ at the boundary after packing transition. Approaching the center from the boundary, $\langle\delta_l\rangle_m$ increases, so the local dryout region is outside the wet region. As shown in (Fig. 5(b)), starting from the center to r_{ld} in a radial direction, only wet region exists. From r_{ld} to $L_p'/2$, the local dryout region is encountered with wet region, and thus, local dryout and wet region are distributed in the monolayer. In the partially dry regime, $\langle q\rangle$ increases and $A\langle R_t\rangle_m$ decreases rapidly with decreases in $\langle T_s - T_{\rm lg}\rangle$ (Fig. 6) [11]. These are predicted by the network model (Eqs. (20)–(27)) and change of heat flow rate absorbed in local dryout region as

$$\begin{cases} Q_i = qA_{h,i} & \text{where} \quad i \in [1, n_1], \quad r_i \in [D_p/2, r_{ld}] \\ Q_i = c_{ld}qA_{h,i} & \text{where} \quad i \in [n_1+1, n_2], \quad r_i \in [r_{ld}, r_{cd}] \\ Q_i = qA_{h,i} = 0 & \text{where} \quad i \in [n_2+1, N], \quad r_i \in [r_{cd}, L_p'/2]. \end{cases} \tag{12}$$

In this regime, as mentioned, since complete dryout (Fig. 2(d)) does not occur in this regime, $r_{cd} = L_p'/2$, and $N_2 = N$ in Eq. (12). From $D_p/2$ to r_{ld} (wet region, stable meniscus), q is supplied through A_i because evaporation rate increases as q increases. For $r_{ld} \leqslant r_i \leqslant L_p'/2$ (local dryout region), with increase in q, the meniscus becomes unstable, and overall evaporation rate does not increase as much as wet region [33]. A portion of heat flux $c_{ld}q$ is thus absorbed in the locally dry region (Eq. (12)), where c_{ld} is the ratio of liquid volume at close- and loose-packed region, i.e., 0.15.

Corresponding to heat flow rate Q_i, superheat ΔT_i is determined using Fourier's law (Eq. (22)) as

$$\Delta T_i = \frac{Q_i}{A_i}\frac{\langle\delta_l\rangle_{m,i}}{\langle k\rangle_{m,i}} = T_{s,i} - T_{\mathrm{lg},i} \quad i = 1,2,3,\ldots,N. \tag{13}$$

The averaged superheat over heated area then becomes

$$\langle\Delta T\rangle = \frac{\sum_{i=1}^{n_2}\Delta T_i A_i + \sum_{i=n_2+1}^{N}\Delta T_{cd} A_{cd,i}}{A_h}, \tag{14}$$

where supeatheat at complete dryout region ΔT_{cd} is defined as

$$\Delta T_{cd} = \frac{\sum_{i=1}^{n_2}\Delta T_i A_i}{A_h - \sum_{i=n_2+1}^{N} A_{cd,i}}. \tag{15}$$

In Eq. (14), ΔT_{cd} is not considered in the partially dry regime. With Eq. (13), the local superheat T_i is calculated and averaged using Eq. (14) without complete dryout. The single-node prediction differs from the multi-node network with local dryout and experiments (Fig. 6) since the local dryout region is not included in the single-node calculation. As expected, when there is no local dryout, the results from multi-node network model follow the single-node network model (red dashed line in Fig. 6).

The partially dry regime caused by local dryout in monolayer is similar to partial dryout in the bi-porous wicks [9,11,13–16], which have nonlinear thermal resistance (S shape pattern). In bi-porous wicks, the liquid supplied through smaller pores is evaporated with extended surface area caused by the large pores [9,13], which are filled with vapor. Similarly, here in the partially dry regime, the liquid reaches the boundary of screen-post-monolayer unit cell through the close-packed regions and is also evaporated along the way according to the liquid coverage proportion.

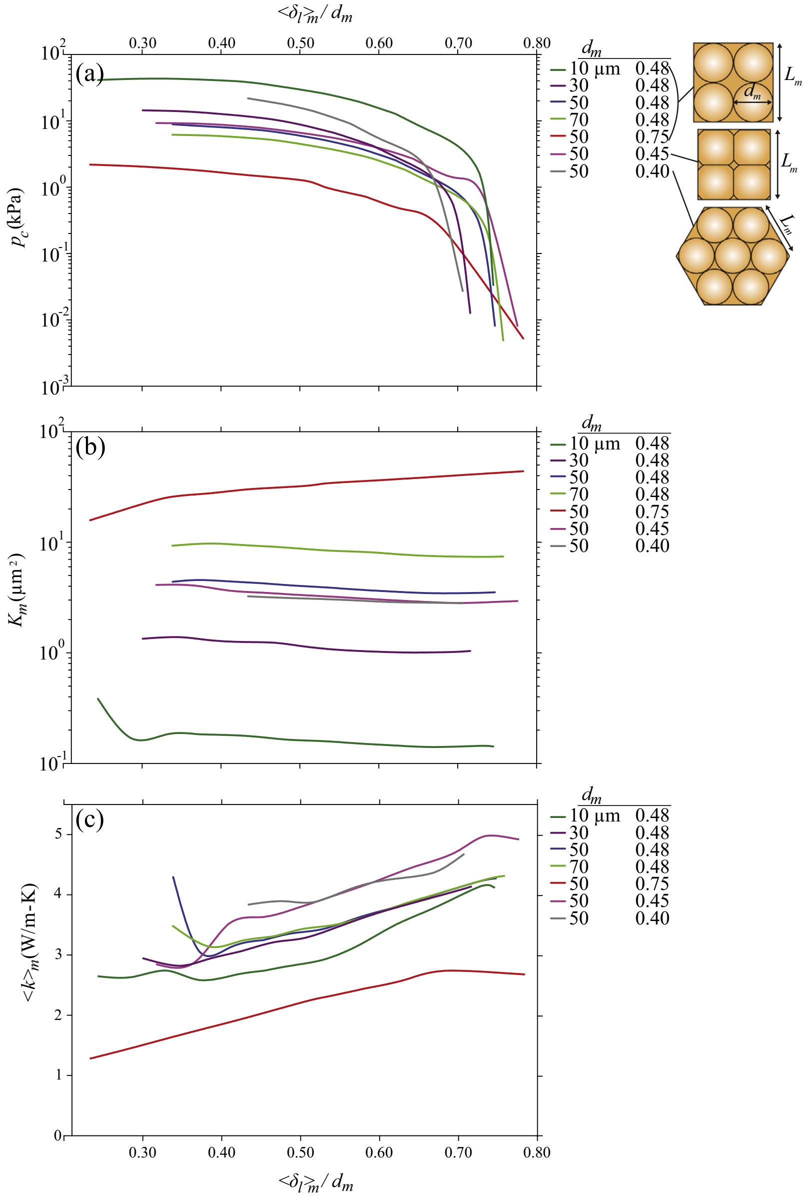

Fig. 7. Variations of predicted (a) capillary pressure, (b) permeability, and (c) thermal conductivity of the homogeneous unit cells in the different monolayers (ϵ = 0.40–0.75), as a function of average liquid thickness. Different particle diameters (10–70 µm) and different packing (square, square with sintering and hexagonal) are used with a contact angle of 45°.

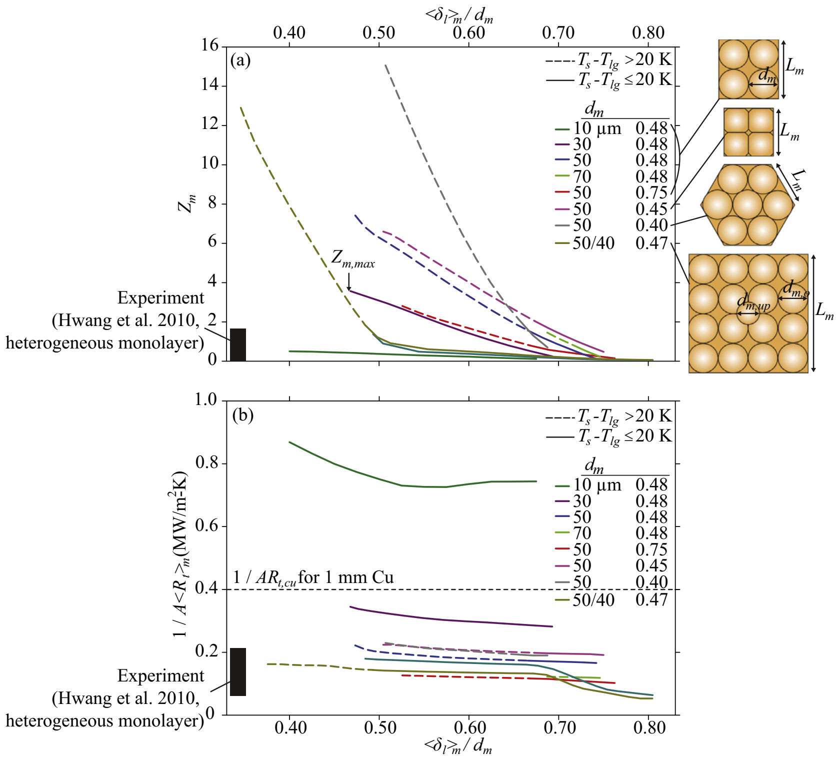

Fig. 8. (a) Dimensionless figure of merit Z_m and (b) thermal conductance $1/A\langle R_t\rangle_m$ with respect to dimensionless average liquid thickness. The dashed line indicates that the superheat exceeds 20 K, and the solid line indicates that superheat is lower than 20 K. The range encountered with the heterogeneous monolayer is marked on the left. Typical receding meniscus dynamics in the homogeneous unit cell during wet regime can be found in the video (click here, Youtube).

With further increases in $\langle q\rangle$ up to 3.5 MW/m^2, the dry-front regime is reached when $\langle\delta_l\rangle_m < 0.4d_{m,o}$. (Figs. 5 and 6). In this regime, the wet ($D_p/2$ to r_{ld}), partially dry (r_{ld} to r_{cd}) and completely dry regions (r_{cd} to $L'_p/2$) coexist. In the last region, the thermal resistance is very large, and so $q = 0$ in Eq. (12). The p_c at the dry front is $p_{lo,max}$, same as the unit cell boundary in partially dry regime. When the wet region disappears at $\langle q\rangle = 15.0$ MW/m^2, the large-superheat regime begins with only local and complete dryout regions (Figs. 5 and 6), and the results show a maximum $\langle q\rangle = 36$ MW/m^2 and a thermal resistance $A\langle R_t\rangle_m = 6.6$ μK/W/m^2 (Fig. 6). In these regimes, the liquid flow path decreases as wet region is dried out, and Δp_m decreases. Since the total liquid pressure drop $\Delta p_m + \Delta p_s + \Delta p_p$ is constant, $\Delta p_s + \Delta p_p$ becomes large with increase in the liquid velocity. More liquid then becomes evaporated with higher evaporation rate, and both $\langle q\rangle$ and $A\langle R_t\rangle_m$ increase with increase in $\langle T_s - T_{\rm lg}\rangle$.

The experiment [4] and predictions made here are compared with the capillary-viscous $\langle q\rangle_{max,c-v}$, hydrodynamic instability (pool boiling) $\langle q\rangle_{CHF,Z}$ and kinetic limits $\langle q\rangle_k$ in Fig. 6. The experiment was up to the superheat of 20 K due to the heater power capability with $\langle q\rangle = 4$ MW/m^2. The capillary-viscous limit is based on the maximum capillary pressure in the monolayer, and is 36 MW/m^2. The hydrodynamic instability (Zuber) limit [34] is

$$q_{CHF,Z} = 0.13\rho_g\Delta h_{\rm lg}\left[\frac{g\sigma(\rho_l-\rho_g)}{\rho_g^2}\right]^{1/4}, \qquad (16)$$

and gives 1.1 MW/m^2 for water at 1 atm. The kinetic limit [34] is

$$q_{max,k} = \left(\frac{R_gT_{\rm lg}}{2\pi m}\right)^{1/2}\rho_g\Delta h_{\rm lg}, \qquad (17)$$

and give 200 MW/m^2 for saturated water at 1 atm. For comparison of thermal resistance we consider a copper substrate (wall) of 1 mm thickness, i.e.,

$$AR_{t,Cu} = \frac{\langle\delta_{l,Cu}\rangle}{k_{Cu}}, \qquad (18)$$

which gives $AR_{t,Cu} = 2.5$ μK/(W/m^2). Critical heat flux in experiment of [4] exceeds $q_{CHF,Z}$, but does not reach $\langle q\rangle_{max,c-v}$, which requires a large-superheat regime with $\langle k\rangle_m$ improvement.

In summary, the flooded regime begins with zero heat flux at $\langle\delta_l\rangle_m = 1.2d_{m,o}$. When $\langle q\rangle$ reaches 1.7 MW/m^2, the wet regime begins with $\langle\delta_l\rangle_m = d_{m,o}$. As $\langle q\rangle$ increases over 2.3 MW/m^2, $\langle\delta_l\rangle_m$ becomes smaller than $0.74d_{m,o}$, and the partially dry regime appears. Up to $\langle q\rangle = 3.5$ MW/m^2, the dry-front regime is reached with $\langle\delta_l\rangle_m = 0.4d_{m,o}$. After over $\langle q\rangle = 15$ MW/m^2, the large-superheat regime appears.

4. Optimal performance of homogeneous monolayer

Using Table 1 properties except for the monolayer, the MAHPS performance is predicted with the multi-node network model varying the monolayer unit-cell structure, and for the wet regime. A homogeneous close-packed unit cell is used to the monolayer since uniform packing delays dryout. As in Section 2, the capillary pressure, permeability, and effective thermal conductivity of homogeneous unit cell are calculated, and shown in Fig. 7 for particle diameters 10–70 μm and different packings (square and hexagonal). For most cases, as $\langle\delta_l\rangle_m$ decreases, p_c and K_m increase while $\langle k\rangle_m$ decreases, which is the general trend (Fig. 4). Fig. 8(a) shows the MAHPS figure of merit Z_m, defined below, as a function of dimensionless average liquid thickness (the homogeneous unit cells are also shown). The fluid property based figure of merit for uniform-wick vapor chamber has been introduced for both liquid and vapor phases and used to find optimal working fluid in [35]. Here Z_m is defined as

$$Z_m = \frac{\langle q\rangle/q_{CHF,Z}}{A\langle R_t\rangle_m/AR_{t,Cu}}. \qquad (19)$$

Fig. 8(b) shows the same for the thermal conductance per unit area ($1/A\langle R_t\rangle_m$). With increasing $\langle q\rangle, \langle T_s - T_{\rm lg}\rangle$ increases, $\langle \delta_l\rangle_m$ decreases, and Z_m and $1/A\langle R_t\rangle_m$ increase. The results show that square-packings with ϵ = 0.48 and d_m = 30 and 50 μm have the best performance. With further sintering, $\epsilon = 0.45$, there is slight improvement in performance. For $d_m = 10$ μm, the thermal conductance is improved, but Z_m does not. In Fig. 7 and with Eq. (10), with decreasing d_m, p_c increases, but K_m decreases more than p_c compensation, so MAHPS operates optimally when the particles are not too small.

Under the current superheat range (0–20 K), $d_m = 30$ μm reaches $Z_m = 3.5$, and $1/A\langle R_t\rangle_m$ = 0.35 MW/m^2-K. This high conductance gives $\langle q\rangle$ = 0.45 MW/m^2, which is 1/40 of $q_{max,k}$. In the experiment of [4], local dryout region in the heterogeneous monolayer contributed on increase of Z_m to 1.75 and $1/A\langle R_t\rangle_m$ to 0.35 MW/m^2-K. However, the homogeneous monolayer can achieve higher Z_m and $1/A\langle R_t\rangle_m$ without local dryout region, which is not controllable. For superheat range (0–50 K), the square- and hexagonal-packing ($d_m = 50$ μm, ϵ = 0.48 and 0.40) have Z_m = 4 and 5. The bi-layered square-packing with $d_{m,o}$ = 50 and $d_{m,up}$ = 40 μm also has $Z_m = 4$.

Also shown in Fig. 8(a) and (b) are the ranges observed with the heterogeneous monolayer in the experiment. From Figs. 6 and 8, the packing uniformity and superheat range play critical roles in the MAHPS performance, and homogeneous close-packed particles with diameter (30–50 μm) are optimal monolayer for the better MAHPS performance.

5. Conclusions

In explaining the nonlinear thermal resistance of the MAHPS experiment of Hwang et al. [4], we used the particle packing-heterogeneity (containing some loose-packed regions) in SEM micrographs, developed unit cell models, and solved the pointwise thermal-hydraulic equations to obtain monolayer properties as a function of receding meniscus. In the receding meniscus dynamics, the flooded, wet, partially dry, dry front, and large superheat regimes were identified. Using the regime transitions between them, local network models were able to predict the experimental results rather closely. Indeed, the packing heterogeneity increases the resistance, even with the rather impressive low resistance of 4.8 μK/(W/m^2) in the partially dry regime.

We then consider the ideal, close-packed homogeneous monolayer, predict its performance presenting the dimensionless figure of merit and thermal resistance(conductance), and optimize them with respect to particle diameter and porosity in the monolayer. Based on the effective properties from the pointwise calculations and the network models for the wet regime, we find that particles of diameter 30–50 μm and close packing result in optimal performance.

Acknowledgment

This work is supported by NSF – USA (Thermal Transport and Processes, CBET16235720). We are also thankful to Rich Bonner and Sean Hoeing of Advanced Cooling Technologies for the monolayer fabrication discussions and the sample.

Appendix A. Multi-node liquid and heat flow network model

For a circular screen-post-wick unit cell with a diameter of L'_p, one-dimensional radial flow is assumed emanating from the post. Due to change in radial velocity (due to cross-sectional area change and evaporation), the radial distance is divided in segments (network model). In ith segment, $p_{c,i}$, $K_{m,i}$, and $\langle k\rangle_{m,i}$ vary with the local $\langle \delta_l\rangle_m$, but constant within the segment $i = 1, \ldots, N$, and Eqs. (4) and (5) are implemented locally with them. At the farthest boundary of the unit cell L'_p, liquid velocity $u_{l,N} = 0$. Liquid flows toward the farthest boundary based on the capillary pressure difference across i to $i+1$, in the form of Eq. (4) (Darcy model), which is given as

$$p_{c,i} = p_{c,i+1} - \mu_l \frac{\Delta r}{K_{m,i+1}} u_{l,i+1}, \tag{20}$$

where Δr is the segment length, and $K_{m,i+1}$ is the averaged permeability of anisotropic components of $\mathbf{K}_{m,i+1}$. Since the liquid mass is conserved, mass difference across each segment is evaporated by heat from the substrate, which can be expressed as

$$Q_i = (\dot{M}_{l,i} - \dot{M}_{l,i+1})\Delta h_{\rm lg}, \tag{21}$$

where mass flow rate cross the ith segment $\dot{M}_{l,i} = \rho_l u_{l,i} A_{c,i}$, with a cross-sectional area $A_{c,i} = \pi r_{p,i}\langle \delta_l\rangle_{m,i}$. Heat flux q is uniform on the heated area A_h, and superheat ΔT_i is provided by heat flow rate Q_i, which can be calculated as

$$Q_i = q_{multi} A_{h,i} = \langle k\rangle_{m,i} A_{m,i} \frac{\Delta T_i}{\langle \delta_l\rangle_{m,i}}, \tag{22}$$

where heated area $A_{h,i} = \pi[(r_i + \Delta r)^2 - r_i^2]$ at radial location $r_i = D_p/2 + i(L'_p - D_p)/(2(N-1))$ and $A_{m,i}$ is the monolayer area covered by liquid in ith segment. $A_{m,i} = A_{h,i}$ when there is full liquid coverage but not when there is local dryout (local dryout changes the behavior of q and $A < R_t >_m$, as function of superheat). Temperature-dependent saturated water properties at 1 atm ($p_{\rm lg}$) are used. In the condenser bi-layer screen wicks, the liquid flows along and across the screens with the its outermost location at saturation liquid pressure ($p_l = p_{\rm lg}$, i.e., zero capillary pressure), and then flows through the post and monolayer wicks with a total liquid pressure drop of $\Delta p_l = p_c$. The cross-flow screen wick pressure drop is calculated using empirical correlations [30] with screen geometrical parameters (number density and diameter of shute and warp wires, tortuosity factor, porosity, and pore diameter in Table 1), which are given as

$$f_{s,\updownarrow} = \frac{8.61}{Re_{s\updownarrow}} + 0.52, \quad f_{s,\updownarrow} = \frac{\Delta p_{s,\updownarrow}\epsilon_s^2 D_{s,po}}{\alpha H_s \rho_l u_{l,s}^2}, \quad Re_{s,\updownarrow} = \frac{\rho_l u_{l,s}}{\mu_l a_s^2 D_{s,po}}, \tag{23}$$

where $f_{s,\updownarrow}$ is a friction factor of screen mesh, and $Re_{s,\updownarrow}$ is Reynolds number of liquid flow in crossing direction. The porosity ϵ_s and surface area to unit volume ratio a_s of screen mesh are written as [30]

$$\epsilon_s = 1 - \frac{\pi n_s n_w}{4H_s}(d_w^2 l_{iw} + d_s^2 l_{is}), \qquad a_s = \frac{\pi n_s n_w}{H_s}(d_w l_{iw} + d_s l_{is}), \tag{24}$$

where for plain square screen wicks, the screen tortuosity factor $\alpha = 1.0$, thickness H_s is a sum of the shute and warp wire diameters $d_{s,sh} + d_{s,wa}$, and porosity $\epsilon_s = 0.68$. Using liquid mass conservation (without evaporation) in the screen and post, the liquid velocity is calculated using the cross-sectional area.

The in-plane screen wick pressure drop is calculated using empirical correlation [31] between friction factor $f_{s,\leftrightarrow}$ and liquid Reynolds number $Re_{s,\leftrightarrow}$ in radial (horizontal) direction as

$$f_{s,\leftrightarrow} = \frac{408 e^{-2.94 N_p}}{Re_{s,\leftrightarrow}}, \tag{25}$$

where $f_{s,\leftrightarrow}$ and $Re_{s,\leftrightarrow}$ are expressed as

$$f_{s,\leftrightarrow} = \frac{\Delta p_{s,\leftrightarrow} d_s \epsilon_s^2}{2 l_s \rho_l u_{l,s}^2 (1-\epsilon_s)\beta}, \quad Re_{s,\leftrightarrow} = \frac{d_s \rho_l u_{l,s}}{\mu_l (1-\epsilon_s)\beta},$$

$$\beta = 1 + \frac{(\frac{1}{2} + \frac{N_p H_s}{w_s})(d_s + D_{s,po})}{\pi d_s S_s}. \tag{26}$$

The packing number $N_p = 1$, and the width of the channel are w_s. The mean crimping factor $S_s = 1.05$ [36], and β is a constant value. The mean temperature of the condenser wall and vapor are used for liquid properties. For the circular unit cell (Fig. 1(b)), the liquid flows only in radial direction. The posts have particle diameter $d_p = 150\ \mu\text{m}$ and porosity $\epsilon_p = 0.35$, and the permeability K_p is calculated using the Carman-Kozeny relation [32] as

$$K_p = \frac{\epsilon_p^3}{180(1-\epsilon_p^2)} d_p^2. \tag{27}$$

The liquid flowing along the posts is at saturation temperature and the pressure drop is calculated from the Darcy law (Eq. (4)) (bulk porous medium behavior). For screen-post-wick unit cell, thermal/hydraulic equilibrium is achieved when the sum of pressure drop by the screen wicks, post, and monolayer wicks $\Delta p_s + \Delta p_p + \Delta p_m$ are equal to $p_{c,N}$, which is the maximum capillary pressure.

References

[1] Y. Nam, S. Sharratt, C. Byon, S.J. Kim, Y.S. Ju, Fabrication and characterization of the capillary performance of superhydrophilic Cu micropost arrays, J. Microelectromech. Syst. 19 (3) (2010) 581–588.

[2] Y. Nam, S. Sharratt, G. Cha, Y.S. Ju, Characterization and modeling of the heat transfer performance of nanostructured Cu micropost wicks, J. Heat Transfer 133 (10) (2011) 101502.

[3] S. Sharratt, C. Peng, Y.S. Ju, Micro-post evaporator wicks with improved phase change heat transfer performance, Int. J. Heat Mass Transfer 55 (21–22) (2012) 6163–6169.

[4] G.S. Hwang, Y. Nam, E. Fleming, P. Dussinger, Y.S. Ju, M. Kaviany, Multi-artery heat pipe spreader: experiment, Int. J. Heat Mass Transfer 53 (13–14) (2010) 2662–2669.

[5] G.S. Hwang, E. Fleming, B. Carne, S. Sharratt, Y. Nam, P. Dussinger, Y.S. Ju, M. Kaviany, Multi-artery heat-pipe spreader: lateral liquid supply, Int. J. Heat Mass Transfer 54 (11–12) (2011) 2334–2340.

[6] T. Semenic, Y.Y. Lin, I. Catton, D.B. Sarraf, Use of biporous wicks to remove high heat fluxes, Appl. Therm. Eng. 28 (4) (2008) 278–283.

[7] T. Semenic, I. Catton, Experimental study of biporous wicks for high heat flux applications, Int. J. Heat Mass Transfer 52 (21–22) (2009) 5113–5121.

[8] D.H. Min, G.S. Hwang, M. Kaviany, Multi-artery, heat-pipe spreader, Int. J. Heat Mass Transfer 52 (3–4) (2009) 629–635.

[9] C.-C. Yeh, C.-N. Chen, Y.-M. Chen, Heat transfer analysis of a loop heat pipe with biporous wicks, Int. J. Heat Mass Transfer 52 (19–20) (2009) 4426–4434.

[10] J.A. Weibel, S.V. Garimella, M.T. North, Characterization of evaporation and boiling from sintered powder wicks fed by capillary action, Int. J. Heat Mass Transfer 53 (19–20) (2010) 4204–4215.

[11] S.C. Wong, J.H. Liou, C.W. Chang, Evaporation resistance measurement with visualization for sintered copper-powder evaporator in operating flat-plate heat pipes, Int. J. Heat Mass Transfer 53 (19–20) (2010) 3792–3798.

[12] Y.S. Ju, M. Kaviany, Y. Nam, S. Sharratt, G.S. Hwang, I. Catton, E. Fleming, P. Dussinger, Planar vapor chamber with hybrid evaporator wicks for the thermal management of high-heat-flux and high-power optoelectronic devices, Int. J. Heat Mass Transfer 60 (1) (2013) 163–169.

[13] J.H. Rosenfeld, M.T. North, Porous media heat exchangers for cooling of high-power optical components, Opt. Eng. 34 (2) (1995) 335–341.

[14] M.P. Mughal, O.A. Plumb, An experimental study of boiling on a wicked surface, Int. J. Heat Mass Transfer 39 (4) (1996) 771–777.

[15] R.R. Williams, D.K. Harris, A device and technique to measure the heat transfer limit of a planar heat pipe wick, Exp. Therm. Fluid Sci. 30 (3) (2006) 277–284.

[16] S.W. Reilly, I. Catton, Improving biporous heat transfer by addition of monoporous interface layer, in: Proceedings of ASME Summer Heat Transfer Conference, San Francisco, CA, 2009, pp. 327–333.

[17] M.a. Hanlon, H.B. Ma, Evaporation heat transfer in sintered porous media, J. Heat Transfer 125 (4) (2003) 644.

[18] S. Sarangi, J.A. Weibel, S.V. Garimella, Quantitative evaluation of the dependence of pool boiling heat transfer enhancement on sintered particle coating characteristics, J. Heat Transfer 139 (2017) 021502.

[19] K.A. Brakke, The surface evolver, Exp. Math. 1 (2) (1992) 141–165. <http://www.tandfonline.com/doi/abs/10.1080/10586458.1992.10504253>.

[20] K.A. Brakke, The Surface Evolver and the stability of liquid surfaces, Philos. Trans. Roy. Soc. Lond. A: Math. Phys. Eng. Sci. 354 (1996) 2143–2157.

[21] M.M. Amrei, H.V. Tafreshi, Effects of pressure on wetted area of submerged superhydrophobic granular coatings. Part II: Poly-dispersed coatings, Colloids Surf. A: Physicochem. Eng. Aspects 481 (2015) 547–560.

[22] S. Adera, D. Antao, R. Raj, E.N. Wang, Design of micropillar wicks for thin-film evaporation, Int. J. Heat Mass Transfer 101 (2016) 280–294.

[23] S. Ravi, R. Dharmarajan, S. Moghaddam, Physics of fluid transport in hybrid biporous capillary wicking microstructures, Langmuir 32 (33) (2016) 8289–8297.

[24] J.L. Hilden, K.P. Trumble, Numerical analysis of capillarity in packed spheres: planar hexagonal-packed spheres, J. Colloid Interface Sci. 267 (2) (2003) 463–474.

[25] L.A. Slobozhanin, J.I.D. Alexander, S.H. Collicott, S.R. Gonzalez, Capillary pressure of a liquid in a layer of close-packed uniform spheres, Phys. Fluids 18 (8) (2006) 082104, http://dx.doi.org/10.1063/1.2236123.

[26] R. Ranjan, J.Y. Murthy, S.V. Garimella, Analysis of the wicking and thin-film evaporation characteristics of microstructures, J. Heat Transfer 131 (10) (2009) 101001. <http://docs.lib.purdue.edu/cgi/viewcontent.cgi?article=1448&context=nanopub>.

[27] R. Ranjan, J.Y. Murthy, S.V. Garimella, A microscale model for thin-film evaporation in capillary wick structures, Int. J. Heat Mass Transfer 54 (1–3) (2011) 169–179.

[28] S. Jeon, C. Byon, Effect of meniscus on the permeability of sintered particle wicks, Appl. Therm. Eng. 107 (2016) 33–34.

[29] S.G. Liter, M. Kaviany, Pool-boiling CHF enhancement by modulated porous-layer coating: theory and experiment, Int. J. Heat Mass Transfer 44 (22) (2001) 4287–4311.

[30] J.C. Armour, J.N. Cannon, Fluid flow through woven screens, AIChE J. 14 (3) (1968) 415–420.

[31] H. Kozai, H. Imura, Y. Ikeda, The permeability of screen wicks, JSME Int. J. 34 (2) (1991) 212–219. <https://www.jstage.jst.go.jp/article/jsmeb1988/34/2/34_2_212/_article/-char/ja/>.

[32] M. Kaviany, Principles of Heat Transfer in Porous Media, second ed., Springer, New York, New York, 1995. <http://link.springer.com/book/10.1007%2F978-1-4612-4254-3>.

[33] S. Harmand, K. Sefiane, N. Lancial, A.M. Benselama, Experimental and theoretical investigation of the evaporation and stability of a meniscus in a flat micro-channel, Int. J. Therm. Sci. 50 (10) (2011) 1845–1852.

[34] M. Kaviany, Essentials of Heat Transfer, Cambridge University Press, 2011.

[35] G. Patankar, J.A. Weibel, S.V. Garimella, Working-fluid selection for minimized thermal resistance in ultra-thin vapor chambers, Int. J. Heat Mass Transfer 106 (2016) 648–654.

[36] C. Li, G.P. Peterson, The effective thermal conductivity of wire screen, Int. J. Heat Mass Transfer 49 (21–22) (2006) 4095–4105.